Superhalo of C 22 reexamined

Downloaded from: https://research.chalmers.se, 2023-05-04 18:36 UTC

Citation for the original published paper (version of record):
Shulgina, N., Ershov, S., Vaagen, J. et al (2018). Superhalo of C 22 reexamined. Physical Review C, 97(6). http://dx.doi.org/10.1103/PhysRevC.97.064307

N.B. When citing this work, cite the original published paper.

research.chalmers.se offers the possibility of retrieving research publications produced at Chalmers University of Technology.
It covers all kind of research output: articles, dissertations, conference papers, reports etc. since 2004.
research.chalmers.se is administrated and maintained by Chalmers Library

(article starts on next page)

Superhalo of ^{22}C reexamined

N. B. Shulgina*
National Research Centre "Kurchatov Institute", Kurchatov sq. 1, 123182 Moscow, Russia and Bogoliubov Laboratory of Theoretical Physics, JINR, 141980 Dubna, Russia

S. N. Ershov
Joint Institute for Nuclear Research, 141980 Dubna, Russia

J. S. Vaagen
Institute of Physics and Technology, University of Bergen, N-5007 Bergen, Norway

M. V. Zhukov
Department of Physics, Chalmers University of Technology, S-41296 Göteborg, Sweden

(Received 9 March 2018; published 12 June 2018)

An unusually large value of the ^{22}C matter radius, extracted by Tanaka *et al.* [Phys. Rev. Lett. **104**, 062701 (2010)] from measured reaction cross sections, attracted great attention of scientific community. Since that time, several experimental works related to the ^{22}C nucleus have appeared in the literature. Some of the experimental data, measured with high accuracy, allow us to fix ^{22}C structure more reliably. Two limiting models reproducing ^{22}C nuclear structure within the three-body cluster approach, that allow us to describe all existing experimental data, are presented. The ^{22}C ground state, continuum structure, and geometry are obtained. With fixed ^{22}C wave function, the prediction for the soft dipole mode in ^{22}C, which is studied in the process of Coulomb fragmentation, is performed.

DOI: 10.1103/PhysRevC.97.064307

I. INTRODUCTION

Comprehensive theoretical studies [2,3] of the ground-state structure of the ^{22}C and reactions cross sections for ^{22}C collision with the ^{12}C target were done a few years before the first experimental data [1] about the ^{22}C structure appeared. In these theoretical works the structure of the ^{22}C nucleus was illuminated as an "ideal s-wave two-neutron halo nucleus" [2] and enhanced reaction cross sections in comparison with ^{20}C were predicted. Varying the s-wave ^{20}C core-n potential, ^{22}C binding energy has been predicted in the range 0.122–0.489 MeV and root-mean-square (rms) matter radius—3.61–4.11 fm [3]. Later on, the experimental claim (2010) by Tanaka *et al.* [1] that the hitherto heaviest known Borromean two-neutron halo nucleus ^{22}C may have a giant matter radius of 5.4 ± 0.9 fm sparked off a lot of theoretical estimations [4–11], including ours [12]. Tanaka and coauthors use a simplified three-body model for ^{22}C, giving a connection between the two-neutron separation energy S_{2n} and the experimental reaction cross section. They come to the conclusion that a very small $S_{2n} \sim 10$ keV is needed even if the two halo neutrons are situated in pure s^2 configuration.

The value of the two-neutron separation energy is not experimentally known and the last (2003) estimate [13] assigns for ^{22}C a rather uncertain value, $S_{2n} = 0.42 \pm 0.94$ MeV. Direct mass measurement [14] puts an upper limit for $S_{2n} \leqslant 360$ keV. Such ambiguity has supported discussions about ^{22}C possibly having an extremely large size.

In our previous article [12], in the absence of experimental data except a huge matter radius [1], we explored how the separation energy S_{2n} influences the spatial extension of an s-dominated Borromean halo nucleus and also other observables that are directly connected to the large size of the ground state. Simulations showed that to reach the experimentally suggested lower boundary for the extracted matter radius, the separation energy S_{2n} of two neutrons in ^{22}C should be of the order of tens keV, while to reach the mean value the binding must be even much weaker. Within the cluster model the spatial extension of the nucleus is directly connected to the distance between the matter and charge center of mass (c.m.) positions. This leads to a swelling of the ^{22}C charge radius due to the ^{20}C core motion about the nuclear c.m., compared with the original charge size of the ^{20}C core. Also, the strength and position of soft dipole excitations are very sensitive to the separation energy, thus to the system's spatial extension. The position of the soft dipole peak moves closer to the three-body threshold with decreasing separation energy S_{2n}. Correspondingly, the separation between the average position of matter and charge distributions becomes larger and the height of the dipole peak is increased in accordance with the nonenergy weighted dipole sum rule. Since the flux of virtual photons peaks at small

*n.b.shulgina@gmail.com

 ©2018 American Physical Society

excitation energies, this results in electromagnetic dissociation cross sections that are very sensitive to the separation energy and can reach huge values for the weak binding. All these far-reaching consequences of a giant matter radius should be tested against experimental data.

Recently (2016) new experimental work appeared [15], where interaction cross section of ^{22}C nuclei on a carbon target at 240 MeV/nucleon had been measured with high accuracy. Using a four-body Glauber model the ^{22}C matter radius of 3.44 ± 0.08 fm was deduced, which is much smaller than the previous value [1]. Togano *et al.* [15] emphasize that these new, higher-precision data provide stronger constraints for assessing the consistency of theories describing weakly bound nuclei.

Besides these data, the longitudinal momentum distribution (LMD) of ^{20}C after ^{22}C fragmentation was measured by Kobayashi *et al.* [16]. In spite of the fact that the accuracy of these older measurements is not so high as in Ref. [15], the LMD results can be used as an additional information to constrain the ^{22}C nuclear structure.

The experiment on proton removal from ^{22}N at 68 MeV/nucleon, performed by Mosby *et al.* [17], showed no evidence for a low-lying state of ^{21}C. Authors have reconstructed the ^{20}C + n decay-energy spectrum and estimated a scattering length limit of $|a_s| \leqslant 2.8$ fm. In principle, the experiment could be used to fix the s-wave ^{20}C-n potential. Unfortunately the accuracy of the experiment is not sufficient, especially in the very low energy range.

The experimental data (2012) on the ^{22}C Coulomb dissociation cross sections on Pb target at 230–240 MeV/nucleon have only been presented in Conference talk [18]. Preliminary data are about 1000 mb, which is large but not extremely large. These experimental data could be used for comparison with theoretical predictions.

In view of the new experimental information it may be worthwhile to review the ^{22}C structure and reactions. For that purpose we describe below the three-body cluster model, which is used for description of the ^{22}C nuclear structure, and discuss the constraints that follow from recent experimental data. Two models for the ^{22}C structure that allow us to describe existing experimental data will be presented. The content of these models is different and they give two limiting cases within which the nuclear structure of ^{22}C nucleus may be found. (The system of units $\hbar = c = 1$ is used in this paper.)

II. THE BOUND STATE MODEL

Following our previous paper [12] we consider ^{22}C as a three-body cluster system (^{20}C + n + n) and use the hyperspherical harmonics method to solve the Schrödinger three-body equation [19,20].

Cluster models assume that the wave function of a nucleus with A nucleons is factorized in a product of two parts, $\Psi(\mathbf{r}_1,\ldots,\mathbf{r}_A) = \phi(\mathbf{r}_1,\ldots,\mathbf{r}_{A_C})\,\psi$. The first $\phi(\mathbf{r}_1,\ldots,\mathbf{r}_{A_C})$ is the core wave function describing the motion of the A_C nucleons within the core. The second, ψ describes the relative motion of the ^{20}C core c.m. and the halo nucleons, the cluster constituents.

For three-body cluster models ψ depends on two translational invariant Jacobi coordinates $(\mathbf{x},\mathbf{y})$, where $\mathbf{x}$ is the relative distance between two constituents, and $\mathbf{y}$ is the relative distance between the c.m. of a pair of two constituents and the third fragment.

Let $\{i,j,k\}$ (1, 2, C for halo neutrons and core) numerate the constituents of the three-body model, where $\mathbf{r}_{1,2}$ describe the halo neutron's coordinates in an arbitrary system and $\mathbf{r}_C$ denotes the position of the core c.m.. The normalized Jacobi coordinates for the distance $\mathbf{x}$ between the two constituents $\{j,k\}$, and $\mathbf{y}$ between the c.m. of the pair and the third fragment $\{i\}$, as well as the nuclear center of mass coordinate $\mathbf{R}_{\mathbf{c.m.}}$, are related by

$$\begin{aligned}
\mathbf{x} &= \sqrt{\frac{A_j A_k}{A_{jk}}}(\mathbf{r}_j - \mathbf{r}_k), \quad A_{jk} = A_j + A_k,\\
\mathbf{y} &= \sqrt{\frac{A_i A_{jk}}{A}}\left[\mathbf{r}_i - \frac{1}{A_{jk}}(A_j\mathbf{r}_j + A_k\mathbf{r}_k)\right],\\
\mathbf{R}_{\mathbf{c.m.}} &= \frac{1}{A}(A_i\mathbf{r}_i + A_j\mathbf{r}_j + A_k\mathbf{r}_k), \quad A = A_i + A_j + A_k.
\end{aligned} \tag{1}$$

Here, $A_{1,2} = 1$, A_C, and $A = (A_C + 2)$ are masses (in units of the nucleon mass m, which in our calculations equals the mean value of proton and neutron masses) of halo neutrons, the core, and the halo nucleus, respectively. For two-neutron halo nuclei only two different Jacobi coordinate systems exist since the two valence neutrons are identical particles. One, labeled $\mathbf{T}$ (cluster representation), corresponds to the case when the relative distance $\mathbf{x}$ is between the two halo neutrons. In the second case, called $\mathbf{Y}$ (shell-model representation), the relative distance $\mathbf{x}$ is between core C and one of neutrons. To simplify notation we use the same letters $\mathbf{x}$,$\mathbf{y}$ for different Jacobi coordinates.

The bound state wave function $\psi(\mathbf{x},\mathbf{y})$ that describes relative motion of the cluster constituents is characterized by the total angular momentum J and its projection M on a quantization axis. The $\psi_{JM}(\mathbf{x},\mathbf{y})$ is a solution of the Schrödinger three-body equation,

$$(\hat{H} - E)\,\psi_{JM}(\mathbf{x},\mathbf{y}) = 0, \tag{2}$$

with Hamiltonian for three clusters given by

$$\hat{H} = \hat{T} + \hat{V}_{\mathrm{Cn}}(\mathbf{r}_{C1}) + \hat{V}_{\mathrm{Cn}}(\mathbf{r}_{C2}) + \hat{V}_{\mathrm{nn}}(\mathbf{r}_{12}), \tag{3}$$

where $\hat{T}$ is the kinetic energy operator for relative motion of the constituents, and $\hat{V}_{\mathrm{Cn}}$ and $\hat{V}_{\mathrm{nn}}$ are the binary core-neutron and neutron-neutron interactions, respectively. The binary potentials depend on vectors $\mathbf{r}_{ij} = \mathbf{r}_i - \mathbf{r}_j$ that are relative distances between constituents. Solutions of Eq. (2) at a negative energy ($E = -S_{2n} < 0$) define the bound states of the halo nucleus.

For description of the wave function $\psi_{JM}(\mathbf{x},\mathbf{y})$ we apply the method of hyperspherical harmonics [19]. In this method the relative Jacobi coordinates $(\mathbf{x},\mathbf{y})$ are mapped into (ρ,Ω_ρ), the hyperradius ρ and the set of five-dimensional angular variables $\Omega_\rho = \{\alpha_\rho,\hat{\mathbf{x}},\hat{\mathbf{y}}\}$. The hyperradius ρ and hyperangle α_ρ are introduced by the following relations:

$$\begin{aligned}
\rho^2 &= x^2 + y^2,\\
\alpha_\rho &= \arctan(x/y), \quad 0 \leqslant \alpha_\rho \leqslant \pi/2,
\end{aligned} \tag{4}$$

i.e., $x = \rho \sin\alpha_\rho$, $y = \rho \cos\alpha_\rho$.The hyperradius ρ reflects the size of the three-body system and is the same in any system of Jacobi coordinates. The angular variables Ω_ρ depend on the selection of Jacobi coordinate system.

The wave function ψ_{JM} is decomposed [19] on hyperspherical harmonics

$$\psi_{JM}(\mathbf{x},\mathbf{y}) = \frac{1}{\rho^{5/2}} \sum_{K\gamma} \chi^J_{K\gamma}(\rho)\, \mathcal{J}^{JM}_{K\gamma}(\Omega_\rho), \tag{5}$$

where the five-dimensional hyperharmonic $\mathcal{Y}^{l_x l_y}_{KLM_L}(\Omega_\rho)$ has the explicit form

$$\mathcal{J}^{JM}_{K\gamma}(\Omega_\rho) = \left[\mathcal{Y}^{l_x l_y}_{KL}(\Omega_\rho) \otimes \chi_S\right]_{JM}, \tag{6}$$

$$\mathcal{Y}^{l_x l_y}_{KLM}(\Omega_\rho) = \Psi^{l_x l_y}_K(\alpha_\rho)\left[Y_{l_x}(\hat{\mathbf{x}}) \otimes Y_{l_y}(\hat{\mathbf{y}})\right]_{LM}, \tag{7}$$

with the hyperangular function $\Psi^{l_x l_y}_K(\alpha_\rho)$ defined in Ref. [19]. The hyperharmonics $\mathcal{Y}^{l_x l_y}_{KLM_L}(\Omega_\rho)$ provide a complete orthogonal set of functions defined on the five-dimensional sphere of unit hyperradius. Here, K is the hypermoment, $\gamma = \{S, L, l_x, l_y\}$ is an abbreviation for a set of quantum numbers, which characterize the relative motion of the three-fragments (l_x, l_y are the relative orbital angular momenta for x and y motions, L is the total orbital momentum), χ_{SM_S} is the spin function of the halo neutron pair with spin S and its projection M_S, core spin equals zero.

Inserting decomposition Eq. (5) into the Schrödinger Eq. (2) and projecting out the hyperharmonics $\mathcal{Y}^{l_x l_y}_{KLM}(\Omega_\rho)$, we can get a set of coupled K-harmonic equations for the hyperradial part $\chi^J_{K\gamma}(\rho)$,

$$\left\{-\frac{1}{2m}\left[\frac{d^2}{d\rho^2} - \frac{\mathcal{L}(\mathcal{L}+1)}{\rho^2}\right] - E\right\}\chi^J_{K\gamma}(\rho) = -\sum_{K'\gamma'} V^J_{K\gamma,K'\gamma'}(\rho)\, \chi^J_{K'\gamma'}(\rho), \tag{8}$$

where $\mathcal{L} = K + 3/2$ and the matrix elements are generated from binary interactions in the following way:

$$V^J_{K\gamma,K'\gamma'}(\rho) = \left\langle \mathcal{J}^{JM}_{K\gamma}(\Omega_\rho)\middle| \hat{V}_{\rm Cn}(\mathbf{r}_{C1}) + \hat{V}_{\rm Cn}(\mathbf{r}_{C2}) + \hat{V}_{\rm nn}(\mathbf{r}_{12})\middle| \mathcal{J}^{JM}_{K'\gamma'}(\Omega_\rho)\right\rangle. \tag{9}$$

The asymptotic behavior for a Borromean three-body halo system in the hyperradius is similar to that of a two-body system in the binary separation, and for a bound state determined by the separation energy

$$\chi^J_{K\gamma}(\rho \to 0) \sim \rho^{\mathcal{L}+1}, \quad \chi^J_{K\gamma}(\rho \to \infty) \sim \exp(-\kappa\rho), \tag{10}$$

where $\kappa = \sqrt{2m|E|}$. The automatic incorporation of the correct three-body asymptotic of bound state wave functions for Borromean systems is one of the advantages of the hyperspherical harmonic method.

Usually the system of the hyperradial Eqs. (8) is solved in the **T** system of Jacobi coordinates since the symmetry under permutation of two valence halo neutrons reduces the number of allowed configurations and leads to smaller dimension of coupled equations compared with the case of the **Y** system where permutation symmetry does not appear explicitly. A unitary transformation between representations in different Jacobi systems can be done by using the Raynal-Revai coefficients [21].

TABLE I. Parameters of the ^{20}C + n potentials. Depths V_i are given in MeV. Radii R_i and diffusenesses a_i are given in units of fm.

Set	V_c	R_c	a_c	V_0	R_0	a_0	V_1
B [2]				43.24	3.39	0.65	25.63
s-wave P1	200	1.46	0.4	23.2	3.01	0.67	
s-wave P2	200	1.46	0.4	16.5	3.01	0.67	
p-waves	200	1.86	0.716	43.24	3.39	0.65	25.63
$d_{3/2}$-wave P1				45.0	3.39	0.65	25.63
$d_{5/2}$-wave P1	43.24	3.39	0.65				25.63
$d_{3/2}$-wave P2				45.95	3.39	0.65	25.63
$d_{5/2}$-wave P2	43.24	3.39	0.65				25.63

III. CALCULATIONS

A. Choice of intercluster potentials

Within a cluster three-body (^{20}C + n + n) model the bound state properties of ^{22}C are defined by the intercluster potentials. The main problem in selecting binary potentials between the constituents, is the absence of reliable experimental information about the neutron-core system, beyond the fact that a bound state of ^{21}C does not exist. At present time the only experiment which can be used to reconstruct a core-n potential is the single-proton removal reaction from a beam of ^{22}N done (2013) by Mosby *et al.* [17]. No evidence for a low-lying state was found, and the reconstructed ^{20}C + n decay-energy spectrum could be described with a s-wave line shape having a scattering length $|a_s| < 2.8$ fm (the best fit to experimental data being $a_s = -0.05$ fm). This means that s-wave interaction is small or nearly zero. Since the experimental data [17] are not very accurate at low energies, an alternative may be possible, in which an s-wave virtual state, situated very close to threshold, avoids registration because registration efficiency is nearly zero in this region. The d-wave interaction cannot be constrained by the experimental data [17] because the quadrupole states are unlikely to be populated in the proton removal reaction from the ^{22}N ground state, which is accepted to have $J^\pi = 0^-$.

As a starting point we use the deep potential by Horiuchi and Suzuki [2] (set B shown in Table I), which implies a shell model ansatz: the ^{20}C core in ^{22}C has closed $d_{5/2}$ subshell. This potential has been chosen for calculations because it gives reasonable geometry of ^{22}C and has the following form:

$$\hat{V}_{\rm Cn}(r) = -V_0 f(r) + V_1(\mathbf{l}\cdot\mathbf{s})\frac{1}{r}\frac{df(r)}{dr} + V_s e^{-\mu r^2}, \qquad f(r) = \frac{1}{1 + e^{(r-R_0)/a}}, \tag{11}$$

where the last Gaussian term in Eq. (11) acts in s-wave only ($V_s = 9.46$ MeV, $\mu = 0.09$ fm^{-2}). This potential has Pauli-forbidden states, which must be considered as already occupied by core nucleons, and blocked for the halo neutrons. Different approximations to the complete antisymmetric approach have been developed within the framework of three-body cluster

models (see, for example, Refs. [22,23], which contain descriptions of different methods and study the consequences of their applications). In fact, the way of Pauli principle treatment should be considered as a part of the few-body model and approximation due to such approach has to be included in the total ambiguity of the used model. Here, the Pauli forbidden states (namely s, p, $d_{5/2}$) are projected out by means of supersymmetric transformation [24] of the potential. As a result, the deep potential for these partial waves gets repulsive core at small distances. We regularize the core, which has singularity at zero radius r, and finally simulate the transformed potential in the following form:

$$\hat{V}_{\rm Cn}(r) = V_{\rm core}(r) - V_0 f(r) + V_1(\mathbf{l}\cdot\mathbf{s})\frac{1}{r}\frac{df(r)}{dr},$$
$$V_{\rm core}(r) = \frac{V_c}{1+e^{(r-R_c)/a_c}}. \quad (12)$$

Here, a core part $V_{\rm core}(r)$ provides a necessary repulsion to get an attractive part which is shallow enough, thus a combined potentials Eq. (12) has one bound state less then the original potential Eq. (11). Simultaneously the new potential is a phase equivalent to the old one.

Let us consider in detail this procedure for different partial waves. For s-wave the starting potential from [2] has two bound states (the second bound state is at energy about 14 keV). After supersymmetric transformation the shape of the new potential is parametrized as shown in Eq. (12). The parameters are given in the second row (marked as "s-wave P1") of the Table I except depth parameter V_0 which is equal to 24.9 MeV. This potential still has one bound state, scattering length a_s is positive and equals to 36 fm. Therefore we reduce V_0 to 23.2 MeV to keep the nucleus ^{21}C unbound. Scattering length for the reduced potential is negative and equals -1680 fm. The corresponding virtual s-state is rather close to threshold and cannot be reliably detected, given the condition in the experiment [17]. This potential is marked as 's-wave P1' in Table I. To obtain a potential with the scattering length, estimated in Mosby *et al.* experiment [17] as $|a_s| < 2.8$ fm, we reduce V_0 to 16.5 MeV. The parameters of this potential are marked as "s-wave P2" in Table I. The s-wave scattering phases for all above mentioned cases are shown in Fig. 1.

P-wave potentials do not play a noticeable role in the ^{22}C structure. However, this interaction can be important, for example, in calculations of ^{22}C Coulomb dissociation. We use a potential, which is phase equivalent to the potential of Horiuchi and Suzuki, with parameters shown in Table I and marked as "p-waves."

A more complicated procedure was used to fix d-wave potential since the starting deep potential gives Pauli forbidden state in $d_{5/2}$-wave, while $d_{3/2}$ state is allowed. For the $d_{3/2}$-wave we use a slightly deepened Horiuchi-Suzuki potential (marked as "$d_{3/2}$-wave P1" in Table I) to compensate a more shallow s-wave potential. For $d_{5/2}$-wave we construct a phase equivalent potential with parameters shown in Table I as "$d_{5/2}$-wave P1." In an alternative set of potential parameters P2, we use for $d_{3/2}$-wave the potential (marked as "$d_{3/2}$-wave P2" in Table I), which is deeper than in P1 set, but gives the same rms matter

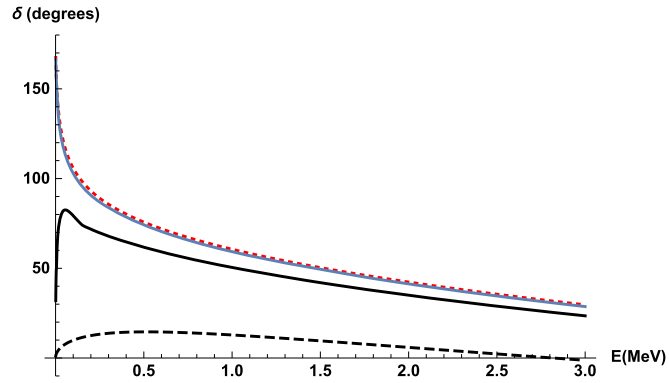

FIG. 1. Phases in ^{20}C-n s-wave scattering. Upper solid line, phases obtained in original deep Horiuchi-Suzuki potential; upper dotted line, in-phase equivalent potential with repulsive core in s-wave; lower solid line, in-P1 potential, providing unbound ^{21}C; lower dashed line, in-P2 potential, based on the experiment [17] by Mosby *et al.*

radius of the ^{22}C nucleus as P1. Scattering phases for $d_{3/2}$-wave are shown at Fig. 2.

In other partial waves, which are all allowed, the ^{20}C-n potential from the Horiuchi and Suzuki paper [2] is used (set B in Table I).

The GPT potential [25], which includes repulsion at small distances, spin-orbit, and tensor forces, has been used for neutron-neutron interactions.

B. Calculated bound state wave functions

The system of the hyperradial Eq. (8) with binary potentials defined above was solved in the **T** system of Jacobi coordinates. Calculations have been performed up to $\rho = 100$ fm with the restrictions $l_x < 4$, $l_y < 4$, and $K_{\rm max} = 20$. Such restrictions ensures that convergence of respective wave function is reached. Two ground-state solutions with binding energies $S_{2n} = 400$ keV and 67 keV were obtained for calculations with potential sets P1 and P2, respectively. These energies are at the different boundaries of the energy region which is compatible with experimental data. Both solutions describe well, as we will see below, the other available experimental data but their

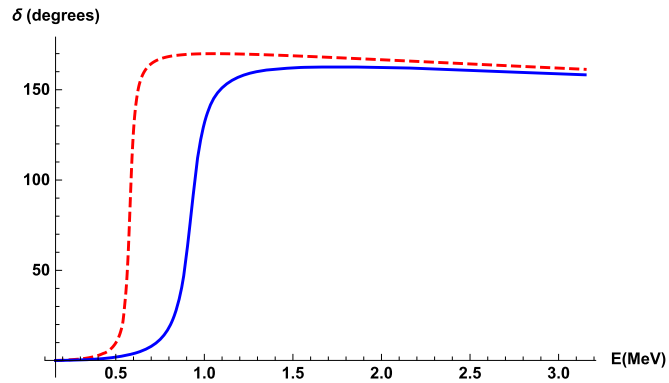

FIG. 2. Phases in ^{20}C-n $d_{3/2}$-wave scattering. Solid line, phases obtained in modified Horiuchi-Suzuki potential P1; dotted line, in-P2 potential, based on the experiment [17] by Mosby *et al.*

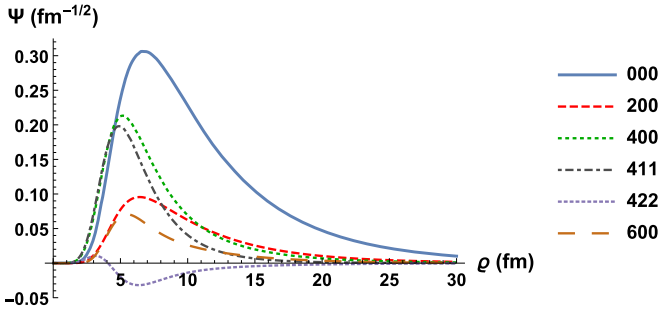

FIG. 3. Main components (K,l_x,l_y) of the ^{22}C wave function for P1 potential.

structure is a quite different. *Thus, we may say, these solutions show the level of ambiguity with which we know the structure of the ground state of the* ^{22}C *nucleus*.

Figures 3 and 4 show the main components of wave functions, calculated with P1 and P2 potentials, respectively. These six components exhaust about 98% of the total normalization. Observables including geometric characteristics, obtained for these wave functions, are listed in the Table II. They include matter $R_{\rm mat}$ and charge $R_{\rm ch}$ radii of the ^{22}C nucleus, that have been obtained with the ^{20}C matter and charge radii equal 2.98 fm. Also shown is the distance R_C of the core c.m. from c.m. of the nucleus, the distance $R_{C(\rm nn)}$ between the core and c.m. of the two halo neutrons, the distance $R_{\rm nn}$ between two halo neutrons, and the distance $R_{\rm Cn}$ of a halo neutron from core. In spite of similar description of the integral spatial characteristics shown in Table II, from Figs. 3 and 4 follow that the two solutions have different partial wave structures. To better demonstrate these differences, weights of different wave function components in the **Y** system in j-j coupling are given in Table III. This representation corresponds to the usual "shell-model" picture of the nuclear structure. The numbers given in Table III demonstrate that the s- and d-motion modes dominate in the nuclear structure and amount together to more than 90% of the total weight. In the deep solution (P1) the s-motion dominates (65%) while in the shallow solution (P2) the $d_{3/2}$ is the main component (60%). Such behavior has a simple explanation if we remember that both wave functions have a similar overall geometric characteristic. Then the more compact deep solution must contain a larger portion of the s-motion while a more shallow diffuse solution must include a larger part of the d-motion. That is why we call these two solutions limiting cases for description of ground state structure of the ^{22}C nucleus.

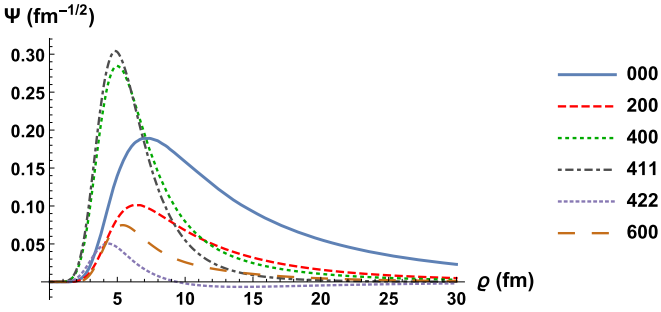

FIG. 4. Main components (K,l_x,l_y) of the ^{22}C wave function for P2 potential.

TABLE II. The binding energy S_{2n} and geometric characteristics of the ^{22}C ground state for calculations with potentials sets P1 and P2. Energy is given in MeV units, radii characteristic in fm. The row "angle" means the average angle between two halo neutron radii counted from c.m. position of ^{22}C. The row $S=0$ shows weight of wave function components with spin $S=0$.

Observable	P1	P2
S_{2n}	0.400	0.067
$R_{\rm mat}$	3.37	3.37
$R_{\rm ch}$	3.00	3.00
R_C	0.461	0.466
$R_{C(\rm nn)}$	5.07	5.13
$R_{\rm nn}$	7.10	6.93
$R_{\rm Cn}$	6.19	6.19
Angle	71°	70°
$S=0$	86%	69%

Figure 5 shows the ^{22}C correlation density in the **T** system, calculated with P1 potential. A prominent dineutron component, forming at relatively large distances between core and two neutron center of mass appears, and a small sigarlike configuration, where neutrons are situated at large distances on opposite sides of the core. Correlation density calculated with P2 potential looks similarly.

C. Fragmentation cross sections and longitudinal momentum distribution (LMD)

Note again, that the wave function content and binding energy for the two potentials are very different, but corresponding geometry is very similar. If we had more accurate experimental data on binding energy we could make a choice at this stage already. However, in the absence of exact data on binding energy we are going to compare our results for reaction cross sections with the precise reaction data [15]. Thus, we fit P2 potential in $d_{3/2}$-wave to get the same rms matter radius for both potentials, keeping in mind that a reaction cross-section depends mainly on geometry.

TABLE III. Weights of ground state wave function components (**Y** system, j-j coupling scheme) of the ^{22}C nucleus for calculations with two versions of the potential.

Version Component	P1 (%)	P2 (%)
$s^2_{1/2}$	64.98	31.63
$p^2_{1/2}$	1.89	2.27
$p^2_{3/2}$	3.83	4.67
$d^2_{3/2}$	27.19	59.04
$d^2_{5/2}$	0.57	0.70
$f^2_{5/2}$	0.65	0.72
$f^2_{7/2}$	0.87	0.96

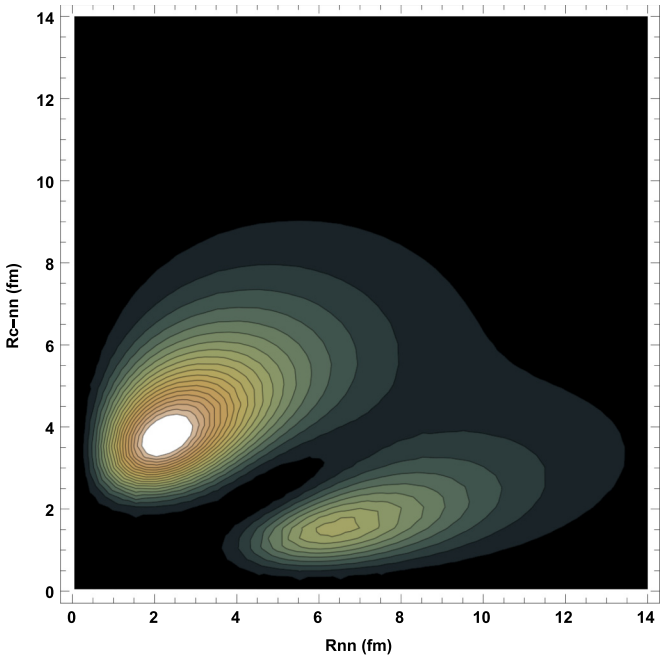

FIG. 5. The ^{22}C correlation density for P1 potential.

For calculation of the cross sections an integration of the wave function with profile functions according to well-known formulas, given in the Appendix, has been performed. The calculated partial cross sections at 240 MeV/nucleon beam energy and the experimental data given in Refs. [15,16] are shown in Table IV.

It should be noted that a modified Horiuchi-Suzuki potential (P1) provides a ^{22}C wave function, which gives the experimental reaction cross section [15] without any additional fitting. The potential P2, motivated by the experiment of Mosby *et al.* [17] and fitted to give the same geometry as the P1 potential, describes the experimental reaction cross section within experimental error bars. So, both wave functions meet experimental data on ^{22}C reaction cross section, measured with high accuracy. In the same paper [15], the experimental data on reaction cross section of the ^{20}C core on the same target at 280 MeV/nucleon is given as $1111 \pm 8 \pm 9$ mb, which we recalculated for beam energy 240 MeV/nucleon, giving $\sigma_R = 1115$ mb. If our three-body approach to ^{22}C is valid, the reaction cross sections for ^{22}C and ^{20}C allow to estimate a two-neutron removal cross section σ_{-2n} as [26,27]

$$\sigma_{-2n} < \sigma_R(^{22}\mathrm{C}) - \sigma_R(^{20}\mathrm{C}_{\mathrm{free}}). \tag{13}$$

In contrast to the free ^{20}C nucleus, the core ^{20}C inside ^{22}C moves around the common center of mass and its effective radius grows. From the experimental data [15], it follows that $\sigma_{-2n} < 165 \pm 46$ mb. Reaction cross sections of ^{20}C core inside ^{22}C nucleus were calculated in Glauber model for P1 and P2 wave functions and are equal to 1141 and 1172 mb, correspondingly. So, the core motion contributes to the reaction cross section at the level of 30–50 mb. The same result was obtained for ^{11}Li in the paper [28].

Other data on two-neutron removal cross section has been reported in the paper [16], $\sigma_{-2n} = 266(19)$ mb. This value evidently contradicts to $\sigma_{-2n} < 165 \pm 46$ mb, deduced from the experimental work [15]. However, σ_{-2n} in the paper [16] seems to be obtained in a model dependent way (see Eq. (1) in Ref. [16]). "To do so total reaction cross sections of 1375 mb for ^{22}C, 1090 mb for ^{20}C..., which were estimated using eikonal calculations, were employed." A theoretical reaction cross section of 1375 mb for ^{22}C is much larger than experimental value $1280 \pm 22 \pm 7$ mb, while a theoretical reaction cross section of 1090 mb for ^{20}C is lower than experimental value $1111 \pm 8 \pm 9$ mb. Therefore, the deduced σ_{-2n} appears to be as large as 266(19) mb. Besides contradictory two neutron removal cross section, ^{20}C longitudinal momentum distribution (LMD) after fragmentation on ^{12}C target has been obtained. Although the accuracy of LMD is not very high, we try to test our wave functions against these new data.

It was pointed out by Bertulani and McVoy [29] that the longitudinal component of the momentum (taken along the beam or z direction) gives the most accurate information on the intrinsic properties in the halo and that it is insensitive to details of the collision and the size of the target. The shape of the momentum distribution reflects the momentum content in halo part of total wave function. Since the experimental cross section of two neutron removal [16] is controversial, we compare with experimental data only the *shape* of LMD. Unfortunately, the experimental shape [16] is not very precise either. Taking into account all these circumstances, to get the LMD shape we restrict ourselves to the Fourier transform of the ^{22}C wave function:

$$\frac{d\sigma}{d\mathbf{k}_{y\parallel}} \sim \left| \int d\mathbf{x}\, d\mathbf{y}\, \exp(-\imath(\mathbf{k}_{y\parallel} \cdot \mathbf{y}_{\parallel}))\psi_{JM}(\mathbf{x},\mathbf{y}) \right|^2. \tag{14}$$

The ^{20}C momentum $\mathbf{p}$ is connected to $\mathbf{k}_y$ by the relation $\mathbf{p} = \sqrt{20/11}\,\mathbf{k}_y$. The results of calculations are shown in Fig. 6 together with experimental data [16]. The theoretical curves have been corrected for the experimental resolution (27 MeV/c). The shape, obtained with P1 wave function, coincides with experiment perfectly, except from a minor disagreement at very high momenta. The shape, obtained with P2 wave function, fits experimental data less, thus demonstrating sensitivity to the wave function content. We recall, that the P1 wave function contains about 65% of s-wave and 30% of d-wave while

TABLE IV. ^{22}C fragmentation cross sections on ^{12}C target at 240 MeV/nucleon beam energy: two-neutron stripping σ_{0n}, one-neutron stripping σ_{1n}, diffraction σ_{2n}, two-neutron removal cross section σ_{-2n}, and reaction cross section σ_R. All cross sections are given in mb.

Value	σ_{0n}	σ_{1n}	σ_{2n}	σ_{-2n}	σ_R
Theory P1	8	109	31	148	1283
Theory P2	7	92	21	120	1293
Experiment				266(19) [16]	$1280 \pm 22 \pm 7$ [15]

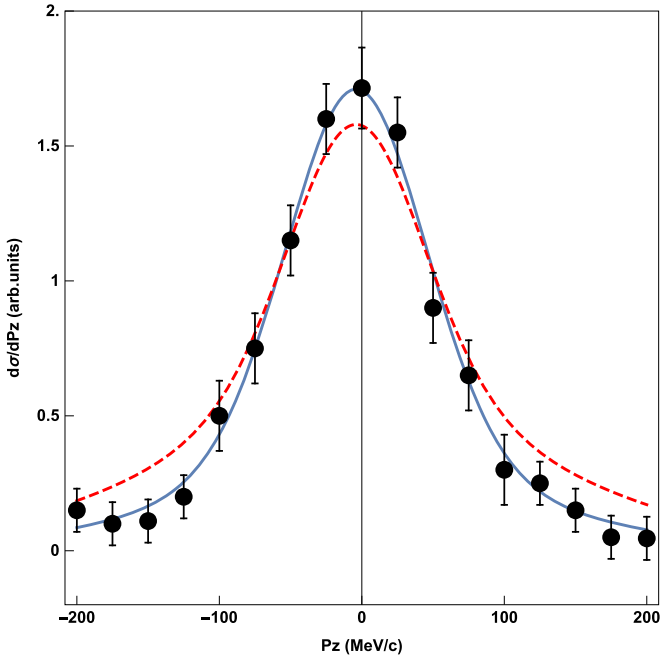

FIG. 6. Longitudinal momentum distribution of ^{20}C core after ^{22}C fragmentation on ^{12}C target for P1 potential (solid line) and for P2 potential (dashed line). Points are experimental data from Ref. [16].

the P2 wave function contains about 27% s-wave and 60% d-wave. Large amount of d-wave in P2 wave function leads to wide wings of LMD. For P1 wave function the FWHM is equal to 78 MeV/c, while for P2 it is equal to 75 MeV/c. This is illustrated at Fig. 7, where the original LMD (without corrections for experimental resolution) are shown for different hyperangular momentum contents. The shape is seen to be very sensitive to wave function structure.

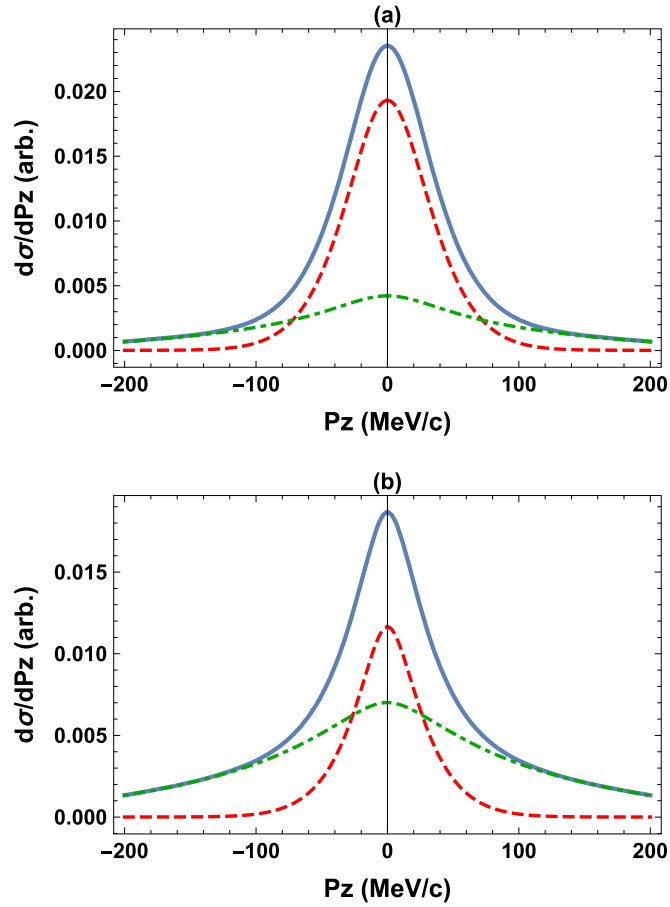

FIG. 7. Longitudinal momentum distribution of ^{20}C core after ^{22}C fragmentation on ^{12}C target for P1 potential (a) and for P2 potential (b). Solid lines, total LMD; dashed line, K = 0 contribution; dash-dotted line, $K > 0$ contribution. Both LMD are normalized to unity.

D. Soft dipole mode and Coulomb dissociation

Characteristics of nuclear halos are revealed not only in the specific structure of the ground state (loosely bound, abnormal spatial extension with extreme clusterization) but also in low-energy excitations above the breakup threshold where a concentration of transition strength is observed. The most spectacular is the appearance of a soft dipole excitation mode that dominates the electromagnetic dissociation (EMD) cross section. In stable nuclei all dipole excitations are usually concentrated in the giant dipole resonance that corresponds to high-frequency collective proton-neutron vibrations. In neutron halo nuclei all charges are concentrated in the core, thus the charge and matter c.m. do not coincide and low-frequency dipole oscillations of the halo neutrons against the core may easily be excited. Historically the large Coulomb dissociation cross sections for ^{11}Li incident on heavy targets were predicted [30] by assuming that the ^{11}Li nucleus is composed of a ^{9}Li core and a point di-neutron, and subsequently confirmed experimentally (see, for example, Ref. [31]). Existence of a new low-lying dipole resonance mode (the so-called soft dipole mode) in such systems was suggested by Ikeda [32]. It should be noted that at least for the lightest Borromean halo nuclei ^{6}He and ^{11}Li, the low-lying dipole excitation mode is not a resonant one, but a more general three-body low-lying continuum response [33] (see also Ref. [34]) where the same conclusion have been obtained for ^{22}C). The position of the $E1$ peak depends on the properties of the ground state due to its closeness to a breakup threshold. In case of resonance it has to be dependent from the properties of continuum state (position of the resonance pole) but not a ground state.

The electric dipole excitations describe transitions from ground to continuum states by action of the dipole operator. To obtain the E1 strength function we solve the following equation:

$$(\hat{H} - E_f)\psi^{(+)}_{J_f M_f \mu} = \hat{\mathbf{D}}_\mu \, \psi^{(\mathrm{gs})}_{JM} \, , \qquad (15)$$

where E_f is the three body energy in continuum, $\psi^{(\mathrm{gs})}_{JM}$ is the ground-state wave function, obtained from the solution of Eq. (2), and $\psi^{(+)}_{J_f M_f \mu}$ is three-body continuum wave function with outgoing wave boundary conditions. Dipole operator $\hat{\mathbf{D}}$

for two neutrons and core is

$$\hat{\mathbf{D}} = e \sum_{i=1}^{A} Z_i \, |\mathbf{r}_i - \mathbf{R}_{\text{c.m.}}| \, Y_{1\mu}(\hat{r}_i) = e\sqrt{\frac{3}{4\pi}} \, Z_C \, \mathbf{R}_C .$$

The non-energy-weighted sum rule for E1 transition can be written as

$$\int \frac{dB_{E1}(E_f)}{dE_f} \, dE_f = \frac{1}{2J+1} \sum_{\mu M} \left\langle \psi^{(\text{gs})}_{JM} \middle| \hat{\mathbf{D}}^*_\mu \hat{\mathbf{D}}_\mu \middle| \psi^{(\text{gs})}_{JM} \right\rangle = \frac{3}{4\pi} \, e^2 Z_C^2 \left\langle R_C^2 \right\rangle . \tag{16}$$

It is interesting to note that the sum rule value or $\langle R_C^2 \rangle$ is sensitive to correlations. For example, it is possible that the radial extent of neutron wave functions is very large, but $\langle R_C^2 \rangle$ is small (this happens if the neutrons reside on opposite sides of the core, so called "cigar-like" configuration).

In hyperspherical variables $\mathbf{R}_C = -\sqrt{A_{12}/AA_C}\,\mathbf{y}$ and the dipole operator can be written as

$$\hat{\mathbf{D}}_\mu = e \, Z_{\text{eff}} \, \rho \, \cos(\alpha_\rho) \, Y_{1\mu}(\hat{\mathbf{y}}), \tag{17}$$

where $Z^2_{\text{eff}} = Z_C^2 \, A_{12}/A \, A_C = 9/55$. For continuum wave functions, defined as

$$\psi^{(+)}_{J_f M_f \mu} = C^{J_f M_f}_{JM1\mu} \sum_{K_f \gamma_f} \frac{\chi^{J_f}_{K_f \gamma_f}(\varkappa\rho)}{\rho^{5/2}} \mathcal{J}^{J_f M_f}_{K_f \gamma_f}(\Omega_\rho),$$

where $\varkappa = \sqrt{2mE_f}$ and $C^{J_f M_f}_{JM1\mu}$ is the Clebsch-Gordon coefficient, the Schrödinger equation is reduced to

$$\left[\frac{d^2}{d\rho^2} - \frac{(K_f+3/2)(K_f+5/2)}{\rho^2} + 2mE_f\right] \chi^{J_f}_{K_f\gamma_f}(\varkappa\rho) - 2m \sum_{K'_f\gamma'_f} V_{K_f\gamma_f, K'_f\gamma'_f}(\rho) \chi^{J_f}_{K'_f\gamma'_f}(\varkappa\rho) = \Phi^{J_f}_{K_f\gamma_f}(\rho)$$

$$\Phi^{J_f}_{K_f\gamma_f}(\rho) = 2meZ_{\text{eff}} \sum_{K\gamma} \rho \, \chi^J_{K\gamma}(\rho) \left\langle \mathcal{J}^{J_f}_{K_f\gamma_f}(\Omega_\rho) \middle\| \cos(\alpha_\rho) \, Y_1(\hat{\mathbf{y}}) \middle\| \mathcal{J}^J_{K\gamma}(\Omega_\rho) \right\rangle$$

$$= 2meZ_{\text{eff}} \sum_{K\gamma} \rho \, \chi^J_{K\gamma}(\rho) \, (-)^{l_x+S+J} \delta_{SS_f} \, \delta_{l_x l^f_x} \frac{\hat{l}_y \hat{l}^f_y \hat{L} \hat{L}_f \hat{J}}{\sqrt{4\pi}} \begin{Bmatrix} l_x & l_y & L \\ 1 & L_f & l^f_y \end{Bmatrix} \begin{Bmatrix} L_f & S_f & J_f \\ J & 1 & L \end{Bmatrix}$$

$$\times \, C^{10}_{l_y 0 l^f_y 0} \left\langle \Psi^{l^f_x l^f_y}_{K_f}(\alpha_\rho) \middle| \cos(\alpha_\rho) \middle| \Psi^{l_x l_y}_{K}(\alpha_\rho) \right\rangle .$$

This system of equations is solved for the three-body problem as it has been described in Ref. [35]. For calculation of observables the flux of particles through the hypersphere of the large radius is used:

$$\mathcal{F}_{J_f}(E_f) = \frac{1}{m} \, \text{Im} \left[\sum_{K_f\gamma_f} \chi^{J_f *}_{K_f\gamma_f}(\varkappa\rho) \frac{d}{d\rho} \chi^{J_f}_{K_f\gamma_f}(\varkappa\rho) \right] \Bigg|_{\rho\to\infty} = \frac{\varkappa}{m} \sum_{K_f\gamma_f} \left| A^{J_f}_{K_f\gamma_f} \right|^2 . \tag{18}$$

The values $A^{J_f}_{K_f\gamma_f}$ are asymptotic amplitudes defined as

$$\chi^{J_f}_{K_f\gamma_f}(\varkappa\rho) \overset{\rho\to\infty}{=} A^{J_f}_{K_f\gamma_f} \, h^{(+)}_{K_f+2}(\varkappa\rho) \to A^{J_f}_{K_f\gamma_f} \, e^{i\varkappa\rho} .$$

It is easy to show that

$$\int d\rho \sum_{K_f\gamma_f} \left| \Phi^{J_f}_{K_f\gamma_f}(\rho) \right|^2 = \frac{2}{\pi} \, m^2 \int \mathcal{F}_{J_f}(E_f) \, dE_f ,$$

and connection between flux and nonenergy weighted sum rule is

$$\int \frac{dB_{E1}(E_f)}{dE_f} \, dE_f = \frac{1}{2\pi} \sum_{J_f} \frac{2J_f+1}{2J+1} \int \mathcal{F}_{J_f}(E_f) \, dE_f = \frac{1}{2\pi} \sum_{J_f} \frac{2J_f+1}{2J+1} \int \sqrt{\frac{2E_f}{m}} \sum_{K_f\gamma_f} \left| A^{J_f}_{K_f\gamma_f} \right|^2 dE_f . \tag{19}$$

Thus, the strength function for electromagnetic E1 dissociation is obtained as

$$\frac{dB_{E1}(E_f)}{dE_f} = \frac{1}{2\pi} \sum_{J_f} \frac{2J_f+1}{2J+1} \, \mathcal{F}_{J_f}(E_f). \tag{20}$$

The calculations of dipole strength function are shown at Fig. 8 for two ground-state solutions P1 and P2. The hypermoments up to $K_{\max} = 19$ are taken into account in the calculations to

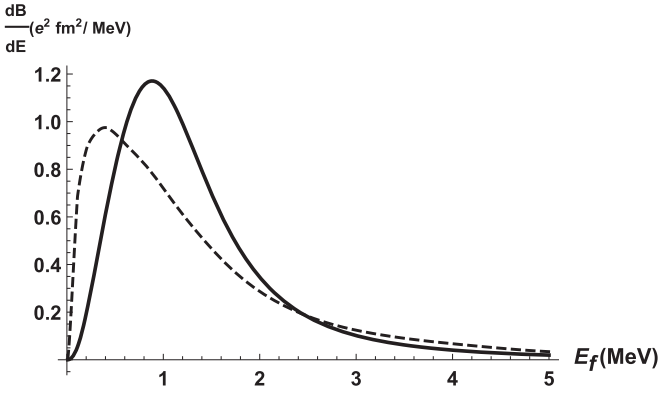

FIG. 8. Calculated ^{22}C dipole strength functions for P1 potential (solid line) and for P2 potential (dashed line).

get convergence of matrix elements. The cluster non-energy weighted sum rule is given in Table V.

Small binding energy for P2 potential (67 keV) leads to shifting of strength function maximum to smaller energies as compared to the P1 case (400 keV). At the same time the large percentage of d-wave in P2 potential makes the strength function wider. Relative contribution of dominant dipole transitions ($s \to p, d \to p, d \to f$) depends on energy of fragments in continuum. For example, at $E_f = 0.5$ MeV the contribution of $s \to p$ transitions for the P2 version is 82%, $d \to p$ transitions—12%, $d \to f$ transitions—4%. At $E_f = 4$ MeV the contributions change drastically to 50%, 47%, and 3%, respectively. We remind, that all these estimates are given in the "shell model" **Y** system. It is interesting to note, that in the low energy range, where a soft dipole mode is expected, the first hyperharmonic in **T** system ($K_f = 1$, $L_f = 1$, $S_f = 0$, $l_x^f = 0$, $l_y^f = 1$) contributes by about 96% to the total strength function.

As we have seen above, the total strength is directly restricted (within the three-body cluster model) by the displacement $\sqrt{\langle|\mathbf{R}_C^2|\rangle}$ of the charge c.m. from the matter c.m. Values of the core displacement for the ^{22}C ground state for different potentials are given in the row R_C of Table II.

Correlations, which can be measured in Coulomb dissociation experiments, depend on energy of fragments in continuum. In Fig. 9 one example is shown at different energies E_f. Here, correlations are plotted as function of $\cos(\theta_k) = (\hat{\mathbf{k}}_x \cdot \hat{\mathbf{k}}_y)$ (linear momenta $\mathbf{k}_x$ and $\mathbf{k}_y$ are conjugated to the Jacobi coordinates **x** and **y**, respectively) and energy ratio E_x/E_f. It is seen from Fig. 9 that neutrons at this energy fly mainly

TABLE V. The cluster nonenergy weighted sum rule of the ^{22}C dipole strength functions calculated for potentials giving different separation energies S_{2n} of the ground state. The sum rule is given for two ranges of the total continuum energy E_f and measured in percent of the computed total sum rule in $e^2 fm^2$ (the column NEWSR)

S_{2n}	$E_f \leqslant 5$ MeV	$E_f \leqslant 10$ MeV	NEWSR
0.400	93.4	96.4	1.826
0.067	86.6	93.0	1.866

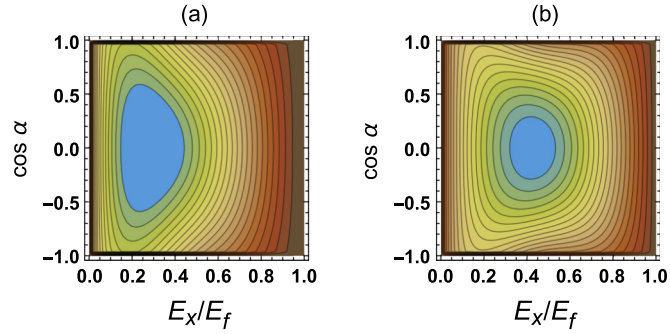

FIG. 9. Correlations for ^{22}C Coulomb dissociation in **T** system for P2 potential at $E_f = 0.5$ MeV (a) and $E_f = 4.0$ MeV (b).

in directions where relative motion ($\mathbf{k}_x$) is a perpendicular to their total momenta ($\mathbf{k}_y$). Correlations at different energies reflect different hyperangular content: at low energy $K = 0$ hyperharmonic dominates, while at $E_f = 4$ MeV $K = 4$ hyperharmonic starts to play a role.

The behavior of the dipole strength functions has strong influence on Coulomb dissociation cross sections when the halo nucleus collides with the heavy target. The estimation of the Coulomb dissociation can be obtained within the framework of first-order perturbation theory [36,37]. According to the virtual photon method, the electromagnetic excitation of the halo nucleus can be described as absorption of virtual photons generated by the target nucleus and defined by the product of the dipole strength function and the spectrum of the virtual photons that peaks at low excitation energies. The Coulomb excitation cross section σ_{E_λ} with multipolarity E_λ is related to the strength function $dB_{E\lambda}/dE_f$ as

$$\frac{d^2\sigma_{E_\lambda}}{dE_f 2\pi b db} = \alpha \frac{(2\pi)^3(\lambda+1)}{\lambda[(2\lambda+1)!!]^2}(E_f + S_{2n})^{2\lambda-1}\frac{dB_{E\lambda}}{dE_f} \times \frac{dn_{E_\lambda}}{db}\mathcal{F}_{\rm abs}(b), \quad (21)$$

where E_f is the energy above the $2n$-emission threshold, S_{2n} is the three-body binding energy, b is the impact parameter related to the scattering angle θ in the laboratory frame (in the quasiclassical approach) as

$$b = a\ \cot(\theta/2),$$

dn_{E_λ}/db is the virtual photon spectrum, which can be defined analytically for $E1$ transitions [36,37]. The factor $\mathcal{F}_{\rm abs}(b)$ in Eq. (21) takes into account a nuclear absorption. In the Bertulani-Baur model it is approximated by the stepwise function at a minimal impact parameter (corresponding to the grazing angle). Here the factor is replaced by a smooth absorption function found within the eikonal approximation of the Glauber model [38,39] as

$$\mathcal{F}_{\rm abs}(b) = \langle\Psi_{\rm gs}||S_n(\mathbf{b},\mathbf{r}_1)S_n((\mathbf{b},\mathbf{r}_2)S_C((\mathbf{b},\mathbf{r}_3)|^2|\Psi_{\rm gs}\rangle$$

Details can be found in the Appendix. Contrary to the original Bertulani-Baur model the integration over impact parameter can't be done analytically. Table VI gives cross sections for the ^{22}C Coulomb dissociation (integrated up to 10 MeV total continuum energy) caused by the collision with a ^{208}Pb target

TABLE VI. Estimation of the E1 Coulomb dissociation cross sections σ_{E1}(mb) for the reaction $^{22}C + ^{208}Pb$ at different beam energies for different $^{20}C - n$ potentials.

E_{beam} (MeV/nucleon)	P1	P2
790	801	888
240	1185	1375
140	1624	1918
40	3357	4337

at different beam energies. The cross sections are given in Fig. 10 for the two versions of the core-n potential—P1 and P2. Especially remarkable is version P2 when the respective Coulomb dissociation cross section is very large.

Cross section of Coulomb and nuclear fragmentation of ^{22}C on ^{208}Pb target at beam energy 240 MeV/nucleon has been measured and preliminary results published in Ref. [18]. Since in the experiment [18] ^{20}C core is registered, the nuclear part here is the two neutron removal cross section σ_{-2n}. According to experimental data, total cross section is about 1500 ± 100 mb. The Coulomb dissociation cross section has been extracted in Ref. [18] by model dependent way and according to Fig. 2 in Ref. [18] is about 900 ± 150 mb. We calculated the total fragmentation cross section (Coulomb + nuclear) on ^{208}Pb at beam energy 240 MeV/nucleon in Glauber model and got 1614 mb for P1 potential and 1751 mb for P2 potential. First result agrees well with the preliminary cross section [18].

In Ref. [34], the ground-state energy, rms radii, and $E1$ strength distribution were calculated within the three-body model in hyperspherical coordinates. Qualitatively this approach is similar to that we used, but the technical realization and calculation details are different. Our model ($P1$) is close to the set 3 (more deeply bound), and our model ($P2$) is similar to the set 1 from the article [34]. Unfortunately, authors did not give any numbers for breakup cross sections but qualitative conclusions on a possible ground state structure and $B(E1)$ distributions are similar to ours. They also remarked that the low-energy peak in the $E1$ distribution is an effect of the low binding of ground state and that it is not a resonance effect.

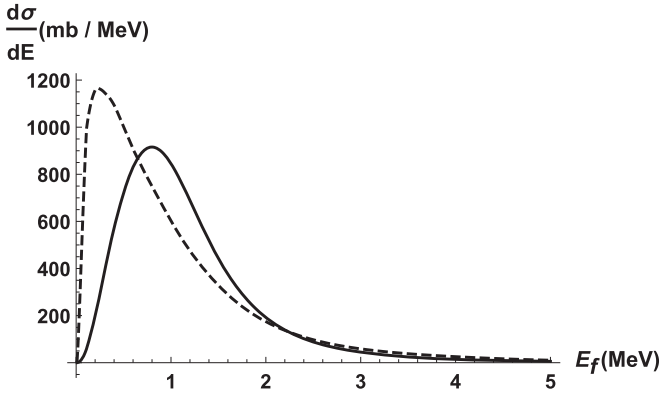

FIG. 10. Calculated ^{22}C Coulomb dissociation cross sections as a function of relative three body energy in continuum for P1 potential (solid line) and for P2 potential (dashed line).

IV. CONCLUSIONS

Given new experimental data (2013, 2016) our previous (2012) investigation of ^{22}C, Ref. [12] has been updated and ^{22}C structure has been determined more reliably. Two limiting versions of ^{20}C core-neutron potentials have been determined, and examined for relevance to existing experimental data. The ^{22}C wave functions, obtained with the two versions of potentials have the same $R_{mat} = 3.37$ fm, but very different separation energy (400 and 67 keV) and (hyper)angular momentum contents. It is well-timed to mention here that accurate experimental data on ^{22}C binding energy is urgently needed for selecting ^{22}C structure.

Since the nuclear reaction cross section mainly depends on geometry, both wave functions give nearly the same reaction cross sections on ^{12}C target (1283 and 1293 mb), which coincide with the very recent (2016) precise experimental data $1280 \pm 22 \pm 7$ mb [15]. Comparison of the two versions with experimental data on ^{20}C longitudinal momentum distribution after fragmentation on ^{12}C target [16], which is sensitive to (hyper)angular momentum contents, shows, that version P1 ($65\% s^2_{1/2}$ and $27\% d^2_{3/2}$) is more preferable than version P2 ($30\% s^2_{1/2}$ and $60\% d^2_{3/2}$). However, the experimental accuracy should be higher to make final decision.

Preliminary results on ^{22}C Coulomb dissociation [18] allow selection of a preferable version. P1 version of core-n potential, providing ^{22}C binding energy of 0.4 MeV meets experimental data within experimental error bars. Energy dependence of Coulomb dissociation cross section is very sensitive to ^{22}C binding energy, which specifies peak position, and to angular momentum content, which defines "width" of the energy distribution. So, it could be very important, if preliminary results [18] could be transformed to final ones.

APPENDIX: PROFILE FUNCTIONS

In this Appendix the profile functions S_{PT} are constructed and fitted to reproduce the experimental cross sections of the ^{22}C constituents on a ^{12}C target. Unfortunately, there is not much experimental data available. We follow here the ideas of Ref. [3] and repeat them briefly. The reaction cross section σ_R and the elastic cross section σ_{el} of the constituent-target collision are calculated by integrating the corresponding probability over the impact parameter $\mathbf{b}$,

$$\sigma_R = \int d\mathbf{b}\,(1 - |S_{PT}(\mathbf{b})|^2), \tag{A1}$$

$$\sigma_{el} = \int d\mathbf{b}\,(|1 - S_{PT}(\mathbf{b})|^2). \tag{A2}$$

The nucleon-target profile function is constructed using the Glauber model as follows:

$$S_n(\mathbf{b}) = \exp\left[-\int d\mathbf{r}_T\,\rho(\mathbf{r}_T)\,\Gamma_{NN}(-\mathbf{r}_{\perp T} + \mathbf{b})\right]. \tag{A3}$$

The nucleon-nucleon profile function Γ_{NN} is usually parameterized in the form

$$\Gamma_{NN}(\mathbf{b}) = \frac{1 - i\alpha_{NN}}{4\pi\beta}\sigma^{tot}_{NN}\exp(-\mathbf{b}^2/2\beta_{NN}), \tag{A4}$$

TABLE VII. The parameters of the nucleon-nucleon profile function.

E beam	α_{nn}	α_{np}	β_{nn}	β_{np}	σ_{nn}(mb)	σ_{np}(mb)
240 MeV/u	0.904	0.526	0.081	0.098	22.40	38.55
790 MeV/u	0.064	−0.210	0.197	0.112	46.69	38.15

where σ_{NN}^{tot} is the total nucleon-nucleon cross section, α_{NN} the ratio of the real to the imaginary part of the NN scattering amplitude, and β_{NN} is the slope parameter of the NN elastic differential cross section. The parameters of the NN profile function are, in principle, subjects to fit, because they can differ from their free values due to in-medium effects like the Pauli blocking and the Fermi motion of nucleons in nuclei.

The density $\rho(\mathbf{r})$ of the ^{12}C target is parameterized using harmonic oscillator wave functions with $l = 0, 1$:

$$\chi_l(r_i) = \frac{\sqrt{2}\, r_i^l \, \exp\left(-r_i^2/2a_i^2\right)}{\sqrt{a_i^{3+2l}\,\Gamma(l+3/2)}}. \tag{A5}$$

The proton density, normalized to the number of protons in the target Z_T, is

$$\rho_p(\mathbf{r}) = \frac{2Z_T(\alpha_p\,(Z_T-2)(r/a_p)^2+2)\exp\left(-r^2/a_p^2\right)}{\pi^{3/2}\,a_p^3\,(3Z_T\alpha_p-6\alpha_p+4)}. \tag{A6}$$

The neutron density can be considered similarly. The parameter $\alpha_{p,n} = 2/3$ has been fixed. The parameters a_p and a_n are fitted to reproduce the charge and matter radii of ^{12}C. The experimental charge radius 2.4829 ± 0.0019 fm [40], and the experimental matter radius 2.35 ± 0.02 fm from Refs. [41,42] have been used in our calculations, leading to $a_p = 1.6868$ and $a_n = 1.5008$.

The Coulomb dissociation calculation needs the ^{208}Pb target parameters. The density $\rho(\mathbf{r})$ of the ^{208}Pb target is parameterized by Wood-Saxon function, fitted to experimental charge radius 5.5 fm:

$$\rho_p(\mathbf{r}) = \frac{0.06308}{1+\exp[(r-6.624)/0.549)]}. \tag{A7}$$

The neutron density can be considered similarly. The proton density is normalized to the number of protons in the target, while the neutron density is normalized to the number of neutrons.

The parameters of the nucleon-nucleon profile function Γ_{NN} are taken from the Refs. [43,44] and smoothly interpolated to the energies of interest and shown in Table VII. Here we distinguish between np- and nn-scattering data.

With the nucleon-nucleon profile function parameters from Refs. [43,44] the n-^{12}C reaction and elastic cross sections at a beam energy of 277 MeV/nucleon are $\sigma_R = 217$ mb and $\sigma_{el} = 70$ mb, which are in perfect agreement with the experimental data [45]. At a beam energy 790 MeV/nucleon we have $\sigma_R = 261$ mb and $\sigma_{el} = 87$ mb, which are also in good agreement with the experiment [45].

The ^{20}C-target profile function is constructed in the optical limit approximation:

$$S_C(\mathbf{b}) = \exp\left[-\int d\mathbf{r}_T\, d\mathbf{r}_P\, \rho(\mathbf{r}_P)\,\rho(\mathbf{r}_T) \times \Gamma_{NN}(\mathbf{r}_{\perp P} - \mathbf{r}_{\perp T} + \mathbf{b})\right], \tag{A8}$$

where the ^{20}C core density $\rho(\mathbf{r}_P)$ is built on harmonic oscillator basis with $l = 0,1,2$. Oscillator parameters $a_p = 2.025$ fm and $a_n = 1.785$ fm are fitted to reproduce the experimental matter radius of ^{20}C, $R_{mat} = 2.98$ fm [15,42], and experimental data for the ^{20}C–^{12}C reaction cross section at 280 MeV/nucleon beam energy [15], which is equal to 1111(29) mb. Now the ^{20}C-target profile function is fixed and we can test it against the experimental data.

The next step is to calculate all observed ^{22}C–^{12}C cross sections and momentum distributions. The formulas for the cross sections are given below:

$$\sigma_R = \int d\mathbf{b}\,(1 - |\langle S_C(\mathbf{b}_C)\, S_n(\mathbf{b}_1)\, S_n(\mathbf{b}_2)\rangle|^2), \tag{A9}$$

$$\sigma_{dif} = \int d\mathbf{b}\,(\langle|S_C(\mathbf{b}_C)\, S_n(\mathbf{b}_1)\, S_n(\mathbf{b}_2)|^2\rangle - |\langle S_C(\mathbf{b}_C)|^2\, S_n(\mathbf{b}_1)\, S_n(\mathbf{b}_2)\rangle), \tag{A10}$$

$$\sigma_{1n} = \int d\mathbf{b}\,\langle|S_C(\mathbf{b}_C)|^2(1-|S_n(\mathbf{b}_1)|^2)|S_n(\mathbf{b}_2)|^2\rangle + \int d\mathbf{b}\,\langle|S_C(\mathbf{b}_C)|^2|S_n(\mathbf{b}_1)|^2(1-|S_n(\mathbf{b}_2)|^2)\rangle,$$

$$\sigma_{0n} = \int d\mathbf{b}\,\langle|S_C(\mathbf{b}_C)|^2(1-|S_n(\mathbf{b}_1)|^2) \times (1-|S_n(\mathbf{b}_2)|^2)\rangle, \tag{A11}$$

where $\langle\ \rangle$ denotes the averaging over the ^{22}C ground state wave function, which is transformed from hyperspherical coordinates ρ, Ω_5 to cartesian ones $\mathbf{x}$,$\mathbf{y}$, and

$$\mathbf{b}_1 = \mathbf{b} - \frac{\mathbf{x}_\perp}{\sqrt{2}} - \frac{\sqrt{5}\,\mathbf{y}_\perp}{\sqrt{11}},$$

$$\mathbf{b}_2 = \mathbf{b} + \frac{\mathbf{x}_\perp}{\sqrt{2}} - \frac{\sqrt{5}\,\mathbf{y}_\perp}{\sqrt{11}},$$

$$\mathbf{b}_c = \mathbf{b} + \sqrt{\frac{1}{220}}\,\mathbf{y}_\perp.$$

Here $\mathbf{x}_\perp$ and $\mathbf{y}_\perp$ are the components of the vectors $\mathbf{x}$ and $\mathbf{y}$ in the plane normal to the incident beam direction.

[1] K. Tanaka, T. Yamaguchi, T. Suzuki, T. Ohtsubo, M. Fukuda, D. Nishimura, M. Takechi, K. Ogata, A. Ozawa, T. Izumikawa, T. Aiba, N. Aoi, H. Baba, Y. Hashizume, K. Inafuku, N. Iwasa, K. Kobayashi, M. Komuro, Y. Kondo, T. Kubo, M. Kurokawa, T. Matsuyama, S. Michimasa, T. Motobayashi, T. Nakabayashi, S. Nakajima, T. Nakamura, H. Sakurai, R. Shinoda, M. Shinohara, H. Suzuki, E. Takeshita, S. Takeuchi, Y. Togano, K. Yamada, T. Yasuno, and M. Yoshitake, Phys. Rev. Lett. **104**, 062701 (2010).

[2] W. Horiuchi and Y. Suzuki, Phys. Rev. C **74**, 034311 (2006).
[3] W. Horiuchi, Y. Suzuki, B. Abu-Ibrahim, and A. Kohama, Phys. Rev. C **75**, 044607 (2007).
[4] M. T. Yamashita, R. S. Marques de Carvalho, T. Frederico, and Lauro Tomio, Phys. Lett. B **697**, 90 (2011); **715**, 282(E) (2012).
[5] H. T. Fortune and R. Sherr, Phys. Rev. C **85**, 027303 (2012).
[6] B. Acharya, C. Ji, and D. R. Phillips, Phys. Lett. B **723**, 196 (2013).
[7] K. Ogata, T. Myo, T. Furumoto, T. Matsumoto, and M. Yahiro, Phys. Rev. C **88**, 024616 (2013).
[8] T. Inakura, W. Horiuchi, Y. Suzuki, and T. Nakatsukasa, Phys. Rev. C **89**, 064316 (2014).
[9] T. Suzuki, T. Otsuka, C. Yuan, and N. Alahari, Phys. Lett. B **753**, 199 (2016).
[10] L. A. Souza, E. Garrido, and T. Frederico, Phys. Rev. C **94**, 064002 (2016).
[11] H. T. Fortune, Phys. Rev. C **94**, 064307 (2016).
[12] S. N. Ershov, J. S. Vaagen, and M. V.Zhukov, Phys. Rev. C **86**, 034331 (2012).
[13] G. Audi, A. H. Wapstra, and C. Thibault, Nucl. Phys. A **729**, 337 (2003).
[14] L. Gaudefroy, W. Mittig, N. A. Orr, S. Varet, M. Chartier, P. Roussel-Chomaz, J. P. Ebran, B. Fernández-Domínguez, G. Frémont, P. Gangnant, A. Gillibert, S. Grévy, J. F. Libin, V. A. Maslov, S. Paschalis, B. Pietras, Yu.-E. Penionzhkevich, C. Spitaels, and A. C. C. Villari, Phys. Rev. Lett. **109**, 202503 (2012).
[15] Y. Togano *et al.*, Phys. Lett. B **761**, 412 (2016).
[16] N. Kobayashi, T. Nakamura, J. A. Tostevin, Y. Kondo, N. Aoi, H. Baba, S. Deguchi, J. Gibelin, M. Ishihara, Y. Kawada, T. Kubo, T. Motobayashi, T. Ohnishi, N. A. Orr, H. Otsu, H. Sakurai, Y. Satou, E. C. Simpson, T. Sumikama, H. Takeda, M. Takechi, S. Takeuchi, K. N. Tanaka, N. Tanaka, Y. Togano, and K. Yoneda, Phys. Rev. C **86**, 054604 (2012).
[17] S. Mosby *et al.*, Nucl. Phys. A **909**, 69 (2013).
[18] T. Nakamura, J. Phys.: Conf. Ser. **381**, 012014 (2012).
[19] M. V. Zhukov, B. V. Danilin, D. V. Fedorov, J. M. Bang, I. J. Thompson, and J. S. Vaagen, Phys. Rep. **231**, 151 (1993).
[20] M. V. Zhukov, B. V. Danilin, D. V. Fedorov, J. S. Vaagen, F. A. Gareev, and J. Bang, Phys. Lett. B **265**, 19 (1991).
[21] J. Raynal and J. Revai, Nuovo Cim. A **68**, 612 (1970).
[22] I. J. Thompson, B. V. Danilin, V. D. Efros, J. S. Vaagen, J. M. Bang, and M. V. Zhukov, Phys. Rev. C **61**, 024318 (2000).
[23] P. Descouvemont, C. Daniel, and D. Baye, Phys. Rev. C **67**, 044309 (2003).
[24] D. Baye, Phys. Rev. Lett. **58**, 2738 (1987).
[25] D. Gogny, P. Pires, and R. de Tourreil, Phys. Lett. B **32**, 591 (1970).
[26] K. Yabana and Y. Ogawa, Y. Suzuki: Nucl. Phys. A **539**, 295 (1992).
[27] Y. Ogawa and K. Yabana, Y. Suzuki. Nucl. Phys. A **543**, 722 (1992).
[28] N. B. Shulgina, B. Jonson, and M. V. Zhukov, Nucl. Phys. A **825**, 175 (2009).
[29] C. A. Bertulani and K. W. McVoy, Phys. Rev. C **46**, 2638 (1992).
[30] P. G. Hansen and B. Jonson, Europhys. Lett. **4**, 409 (1987).
[31] T. Kobayashi *et al.*, Phys. Lett. B **232**, 51 (1989).
[32] K. Ikeda, INS Report JHP-7 (1988), in Japanese.
[33] B. V. Danilin, I. J. Thompson, J. S. Vaagen, and M. V. Zhukov, Nucl. Phys. A **632**, 383 (1998).
[34] E. C. Pinilla and P. Descouvemont, Phys. Rev. C **94**, 024620 (2016).
[35] L. V. Grigorenko, R. C. Johnson, I. G. Mukha, I. J. Thompson, and M. V. Zhukov, Phys. Rev. C **64**, 054002 (2001).
[36] A. Winther and K. Alder, Nucl. Phys. A **319**, 518 (1979).
[37] C. A. Bertulani and G. Baur, Nucl. Phys. A **442**, 739 (1985).
[38] C. A. Bertulani and A. M. Nathan, Nucl. Phys. A **554**, 158 (1993).
[39] W. Horiuchi, S. Hatakeyama, and S. Ebata, and Y. Suzuki, Phys. Rev. C **96**, 024605 (2017).
[40] W. Ruckstuh *et al.*, Nucl. Phys. A **430**, 685 (1984).
[41] I. Tanihata, H. Hamagaki, O. Hashimoto, Y. Shida, N. Yoshikawa, K. Sugimoto, O. Yamakawa, T. Kobayashi, and N. Takahashi, Phys. Rev. Lett. **55**, 2676 (1985).
[42] A. Ozawa, T. Suzuki, and I. Tanihata, Nucl. Phys. A **691**, 599 (2001).
[43] W.-M. Yao *et al.*, J. Phys. G: Nucl. Part. Phys. **33**, 1 (2006).
[44] L. Ray, Phys. Rev. C **20**, 1857 (1979).
[45] W. Bauhoff, At. Data Nucl. Data Tables, **35**, 429 (1986).